
US-JEPA: A Joint Embedding Predictive Architecture for Medical Ultrasound

Ashwath Radhachandran^{1,2} Vedrana Ivezic^{1,3} Shreeram Athreya^{1,4} Ronit Anilkumar¹
 Corey W. Arnold^{1,2,3,4,5,6} William Speier^{1,2,3,5}

Abstract

Ultrasound (US) imaging poses unique challenges for representation learning due to its inherently noisy acquisition process. The low signal-to-noise ratio and stochastic speckle patterns hinder standard self-supervised learning methods relying on a pixel-level reconstruction objective. Joint-Embedding Predictive Architectures (JEPAs) address this drawback by predicting masked latent representations rather than raw pixels. However, standard approaches depend on hyperparameter-brittle and computationally expensive online teachers updated via exponential moving average. We propose US-JEPA, a self-supervised framework that adopts the Static-teacher Asymmetric Latent Training (SALT) objective. By using a frozen, domain-specific teacher to provide stable latent targets, US-JEPA decouples student-teacher optimization and pushes the student to expand upon the semantic priors of the teacher. In addition, we provide the first rigorous comparison of all publicly available state-of-the-art ultrasound foundation models on UltraBench, a public dataset benchmark spanning multiple organs and pathological conditions. Under linear probing for diverse classification tasks, US-JEPA achieves performance competitive with or superior to domain-specific and universal vision foundation model baselines. Our results demonstrate that masked latent prediction provides a stable and efficient path toward robust ultrasound representations.

¹Biomedical AI Research Lab, University of California, Los Angeles, USA ²Department of Bioengineering, University of California, Los Angeles, USA ³Medical Informatics Home Area, University of California, Los Angeles, USA ⁴Department of Electrical and Computer Engineering, University of California, Los Angeles, USA ⁵Department of Pathology, University of California, Los Angeles, USA ⁶Department of Radiology, University of California, Los Angeles, USA. Correspondence to: Ashwath Radhachandran <ashwathradha123@g.ucla.edu>, William Speier <speier@ucla.edu>.

1. Introduction

Self-supervised learning (SSL) has revolutionized the ability to leverage vast unlabeled datasets to build robust foundation models. In particular, masked image modeling (MIM) has emerged as a dominant approach, where models are tasked to reconstruct masked image patches to learn image semantics (Hondru et al., 2025). Although pixel-level reconstruction objectives have proven effective in natural imaging, their utility partially depends on the assumption that local pixel intensities correlate strongly with underlying structural representations. However, when applied to domains characterized by low signal-to-noise ratio and acquisition artifacts, this assumption begins to break down (Xie et al., 2024).

The ultrasound (US) imaging domain is a prime example of this representational bottleneck. US is a critical diagnostic tool in clinical settings, as it is portable, radiation-free, and provides real-time bedside feedback. Yet, image interpretation is difficult due to inherent visual graininess (speckle noise), operator dependence, and substantial variability in acquisition protocols and patient anatomy. In a traditional MIM framework, a generative, pixel-reconstruction objective may force the model to use its representational capacity to model these uninformative, acquisition-dependent features. Since these features, such as blur, acoustic shadow, and pixel-level contrast, vary significantly across clinical environments, a model trained for pixel reconstruction may overfit to these specific noise sources. The resulting significant gap between manually curated training data and real-world settings raises critical concerns about model robustness in out-of-distribution (OOD) scenarios. Without a pretraining objective that prioritizes semantic invariance, US foundation models may fail when subjected to diverse, yet realistic, ultrasound image corruptions.

The challenge of ensuring representational robustness is further compounded by the scarcity of high-quality clinical labels, which are expensive to acquire and require specialized medical expertise. Consequently, there is a need to train foundation models that can extract robust US feature representations and achieve high performance on downstream tasks using minimal supervision. Recent efforts to build US foundation models have attempted to navigate these bot-

tlenecks through domain-specific modifications (Jiao et al., 2024; Megahed et al., 2025; Zhang et al., 2025b). Despite their innovations, these methods ultimately remain anchored to the pixel reconstruction paradigm, potentially underrepresenting the critical global features that distinguish different anatomical regions and pathologies in US.

1.1. Ultrasound Joint Embedding Predictive Architecture (US-JEPA)

To address these challenges, we introduce the Ultrasound Joint-Embedding Predictive Architecture (US-JEPA). Based on Image-based JEPA (I-JEPA), US-JEPA goes beyond the generative pixel-filling paradigm. Instead, it operates entirely in a latent embedding space, predicting the representations of masked target regions from a context block within the same image. By performing feature reconstruction rather than raw pixel reconstruction, US-JEPA can focus on learning global anatomical dependencies and tissue textures.

The I-JEPA framework (Assran et al., 2023) relies on an online teacher updated via Exponential Moving Average (EMA) to guide a gradient-based student with smooth, yet improving targets. This coupling is computationally expensive and sensitive to hyperparameter selection. A core distinction of our framework is the adoption of the Static-teacher Asymmetric Latent Training (SALT) objective (Li et al., 2025), in which a frozen teacher replaces an EMA-updated teacher. US-JEPA uses a frozen, domain-specific teacher, the Ultrasound Representation Foundation Model (URFM) (Kang et al., 2025), to provide stable targets.

URFM previously established the effectiveness of MIM for feature-level reconstruction in ultrasound, performing knowledge distillation from BiomedCLIP (Zhang et al., 2025c), a general-purpose medical vision encoder. URFM’s reconstruction-based objective transfers rich semantic priors to the ultrasound domain, but remains tied to local reconstruction objectives as opposed to global representation consistency. By using URFM as a static teacher, US-JEPA takes a step further by leveraging the SALT latent prediction objective to refine URFM’s ultrasound-specific representations. Rather than just reconstructing missing features, US-JEPA learns to align representations across views within an image. This approach encourages the model to learn the internal physics of US imaging, providing an improved latent space for downstream clinical tasks.

To ensure the model pretrained with US-JEPA is exposed to a wide range of human physiology, we aggregate one of the largest collections of publicly available US imaging to date. After thoroughly searching public repositories, our pretraining dataset encompasses approximately 4.73 million frames from 49 datasets covering 22 distinct anatomies.

1.2. Standardizing Evaluation: UltraBench

A significant challenge in current US foundation model research is the lack of a standardized evaluation protocol. Currently, most studies evaluate on disparate, often private, downstream datasets with non-standardized splits, making rigorous iteration and objective comparison nearly impossible. To promote reproducibility and establish a gold standard for future work, our paper adopts and extends UltraBench (Tupper & Gagné), a publicly available benchmark for US frame-level evaluation. While the original UltraBench provides a strong foundation, we expand its scope to enhance anatomical diversity. Specifically, we include eight classification tasks spanning various organs and pathologies, adding two new tasks for thyroid and breast pathology.

Beyond the dataset benchmark itself, we address a critical gap in previous work: the lack of side-by-side comparisons of available models. To the best of our knowledge, this work is the first to perform an exhaustive linear probing evaluation across all published, publicly available US foundation models. Previous works compare against a limited set of US-specific baselines or rely solely on full fine-tuning, making it difficult to isolate the intrinsic quality of the learned representations. By tuning just a linear head for the classification tasks with a frozen backbone, we provide a standardized assessment of the learned latent space. This rigorous benchmarking ensures that improvements from US-JEPA are measured against a standard and relevant set of baselines, providing a clear map of the current state-of-the-art.

This work takes a significant step forward in ultrasound foundation modeling with the following contributions:

- **JEPA-based US Foundation Model:** We introduce US-JEPA, the first frame-level US foundation model built on JEPA principles.
- **Label-Efficient Representations:** US-JEPA achieves strong linear probing performance with fewer labeled samples than competing baselines.
- **Robustness to Domain-Specific Image Corruption:** Learned representations exhibit increased invariance to ultrasound-specific perturbations in image quality.
- **Comprehensive Benchmarking:** We conduct the most comprehensive linear-probing evaluation to date across publicly available ultrasound foundation models on eight clinical tasks from UltraBench.

2. Related Work

2.1. Universal Vision Foundation Models

While early SSL focused on instance discrimination and contrastive objectives (ex. MoCo (He et al., 2020) and SimCLR (Chen et al., 2020)), the field has expanded to self-

distillation and predictive modeling to capture higher-level semantics. DINO (Caron et al., 2021) demonstrated that student-teacher distillation with Vision Transformers (ViTs) can yield semantically rich features without labels. This paradigm has been scaled by successors, DINOv2 (Oquab et al., 2024) and DINOv3 (Siméoni et al., 2025), to set new benchmarks in universal representation learning. In parallel, I-JEPA (Assran et al., 2023) has proposed moving beyond methods that predict in pixel or token space. By predicting missing latent representations from a visible context, I-JEPA learns the underlying structural logic of an image rather than superficial textures. Despite these universal models excelling on natural images, their direct application to US is limited by modality-specific artifacts, leading research to investigate specialized anatomical and task-based solutions.

2.2. Task-Specific Ultrasound Foundation Models

A significant branch of US research focuses on adapting universal architectures for specific clinical tasks, most notably through the specialization of the Segment Anything Model (SAM) (Kirillov et al., 2023). Works such as SAMUS (Lin et al., 2024) and UltraSAM (Meyer et al., 2025) utilize architectural modifications or large-scale fine-tuning on large segmentation datasets to enable interactive, zero-shot segmentation. Beyond segmentation, SSL has proven useful for US representation learning within specific anatomical systems. In fetal US, UltraDINO (Ambsdorf et al., 2025) outperforms general vision models and USFM by training DINOv2 from scratch on fetal-specific corpora. In the cardiac domain, EchoNet-Dynamic and EchoFM (Ouyang et al., 2020; Kim et al., 2025) use large-scale US video corpora to learn temporal cardiac dynamics and apply these representations to clinical cardiac tasks. These successes demonstrate the power of domain-specific SSL; however, they often rely on curated, task-specific datasets, motivating the need for a robust, general-purpose US foundation model.

2.3. General Ultrasound Foundation Models

The evolution of US foundation models has been defined by a shift from standard pixel-level reconstruction toward domain-aware representation learning. USFM (Jiao et al., 2024) was the first to define the field by training on more than 2 million images (public and private) using a dual spatial-frequency MIM objective, specifically designed to tackle the low spatial resolution and noise inherent in US. Building on this precedent, USF-MAE (Megahed et al., 2025) demonstrated that pre-training exclusively on public US data (using the 370k-image OpenUS-46 corpus) combined with noise-filtering preprocessing, could significantly surpass models initialized on natural images.

More recent efforts have integrated generative refinements and structural priors. For instance, D²MAE (Kang et al.)

uses diffusional deblurring in the MIM framework to address the low SNR inherent to US. EchoCare (Zhang et al., 2025b) leverages a 4.5 million image dataset and introduces a hierarchical classification objective to teach the model nuanced anatomical relationships.

To build on these previous approaches, US-JEPA evolves the feature reconstruction paradigm introduced by URFM. By utilizing this domain-specific teacher and an asymmetric latent objective, US-JEPA is designed to encode the structural logic within US, learning an improved latent space for downstream clinical tasks.

3. Preliminaries

3.1. I-JEPA

The I-JEPA (Assran et al., 2023) architecture consists of a context encoder f_θ , a target encoder \tilde{f}_θ , and a predictor g_ϕ . Given an input image x , the model operates on a sequence of non-overlapping patches. During training, we sample a context block B_c and a set of T target blocks $\{B_i\}_{i=1}^T$, where each block is a subset of patches. From these blocks, we derive disjoint masks M_c and M_i to ensure there is no overlap and prevent a non-trivial prediction task.

The target encoder processes the full image x to produce patch-level representations $\mathbf{s}_y = \tilde{f}_\theta(x)$. The targets for the loss function are defined as the subset of these representations corresponding to the i -th target mask, $\mathbf{y}_i = \mathbf{s}_y[M_i]$. Simultaneously, the context encoder processes only the visible image patches defined by M_c to produce context embeddings $\mathbf{c} = f_\theta(x[M_c])$. The predictor g_ϕ then utilizes these context embeddings, conditioned on mask tokens, p_i , which indicate the target-block locations. The mask tokens are parameterized by a learnable vector with an added positional embedding:

$$\hat{\mathbf{y}}_i = g_\phi(\mathbf{c}, p_i) \quad (1)$$

The training objective is to minimize the Smooth L_1 distance between the predicted $\hat{\mathbf{y}}_i$ and actual \mathbf{y}_i target representations. To prevent representational collapse, I-JEPA employs an asymmetric update rule where the target encoder parameters $\tilde{\theta}$ are an EMA of the context encoder parameters θ .

3.2. Static-teacher Asymmetric Latent Training (SALT)

The SALT paradigm (Li et al., 2025) helps modulate the parameter selection in the JEPA objective by decoupling the student and teacher optimization. SALT demonstrates that a high-performing student can emerge by predicting the latent space of a static teacher, provided the teacher possesses reasonably sufficient semantic priors.

Here, the target encoder h_ψ (ex. an existing foundation

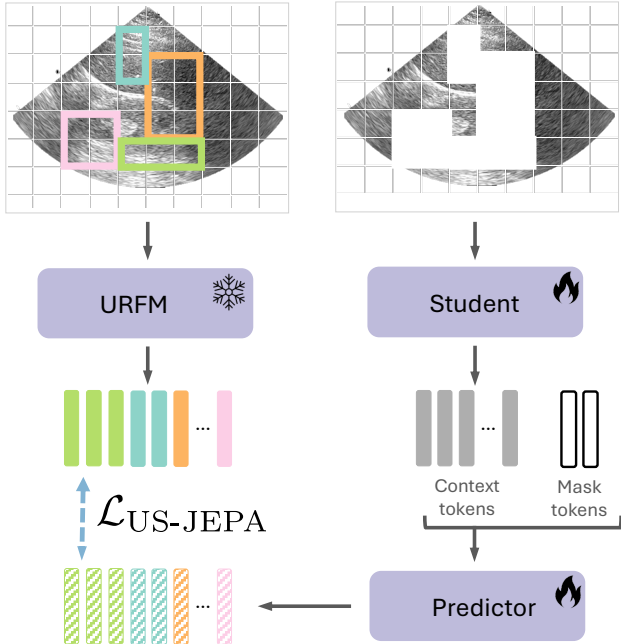


Figure 1. **USrc-JEPA framework.** Here we show the model training framework with USrc. URFM is the frozen teacher that extracts target embeddings. The student and predictor are jointly optimized with $\mathcal{L}_{US-JEPA}$ to align with the target.

model or encoder pretrained via a different objective such as pixel reconstruction) is frozen. The target embeddings \mathbf{y}_i become static conditioned on the input image. Gradients propagate solely through the context encoder f_θ and predictor g_ϕ :

$$\mathcal{L}_{\text{SALT}} = \frac{1}{T} \sum_{i=1}^T \|g_\phi(f_\theta(x[M_c]), p_i) - h_\psi(x)[M_i]\|_1 \quad (2)$$

This approach eliminates the need for the EMA update, thus stabilizing the training dynamics and reducing computational overhead.

4. US-JEPA

US-JEPA (Figure 1) relies on the masked latent objective from I-JEPA to learn the spatial semantics within ultrasound imaging. By forcing the student network to predict missing anatomical structures in a latent space with the guidance of a domain-specific teacher, the model is encouraged to develop a robust feature representation of tissue textures and organ morphology that is invariant to pixel-level noise.

4.1. Self-Distillation via SALT

While the SALT framework has shown that strong students can emerge even from sub-optimal teachers (Li et al., 2025), our goal was to leverage the most robust US representations

to establish a new state-of-the-art. To identify the optimal target provider, we performed an extensive benchmarking of existing US foundation models across UltraBench. Our preliminary results (detailed in Table 2) demonstrate that URFM consistently outperformed other baselines. We select URFM to serve as our frozen teacher and investigate whether the masked latent objective of US-JEPA can achieve better downstream performance, label efficiency in few-shot linear probing and improved stability against domain-specific corruptions.

In our framework, the student context encoder and predictor are optimized to minimize the Smooth L_1 distance between the predicted target embeddings and the URFM target embeddings.

4.2. Ultrasound Region-Conditioning (USrc)

A significant challenge in training on diverse, public ultrasound datasets is the presence of non-anatomical artifacts. Ultrasound frames typically contain peripheral noise, including transducer metadata, intensity scales, patient information, and large black borders. Previous masked imaging approaches rely on raw frames which is suboptimal since it would allow non-ultrasound content to be sampled. We hypothesize that uniform random masking in I-JEPA might inadvertently task the model with predicting these meaningless regions, wasting representational capacity. To test this, we introduce USrc as a spatial prior to isolate the anatomical signal.

Let $x \in \mathbb{R}^{H \times W}$ be the input ultrasound image and $R \in \{0, 1\}^{H \times W}$ be a binary region mask, where $R_{ij} = 1$ denotes valid ultrasound signal and $R_{ij} = 0$ denotes background. We tile the image into non-overlapping patches and define the set of valid patches $\mathcal{P}_{\text{valid}}$ as those containing at least one pixel within R .

Target Sampling: Targets correspond to representations of image blocks. We feed x through the frozen target encoder h_ψ to obtain patch-level representations $\mathbf{s}_y = h_\psi(x)$. We sample T candidate blocks $\{B_i\}_{i=1}^T$ based on scale and aspect ratio constraints. We employ a rejection sampling strategy where a candidate block is accepted only if its intersection with $\mathcal{P}_{\text{valid}}$ exceeds a threshold τ :

$$M_i = B_i \cap \mathcal{P}_{\text{valid}}, \quad \text{subject to } |M_i| \geq \tau \quad (3)$$

The final targets are the representations $\mathbf{y}_i = \mathbf{s}_y[M_i]$.

Context Sampling: We sample a context block B_c with specific scale and aspect ratio constraints. To ensure a non-trivial task, we remove any regions overlapping with the target blocks and apply our overlap constraint:

$$M_c = B_c \cap \mathcal{P}_{\text{valid}}, \quad \text{subject to } |M_c| \geq \tau \quad (4)$$

The masked context $x[M_c]$ is processed by the context encoder f_θ to obtain $\mathbf{c} = f_\theta(x[M_c])$.

Optimization: The training objective is minimized strictly over these anatomical intersections. The predictor aims to minimize the Smooth L_1 distance between the predicted student embeddings and the frozen teacher embeddings:

$$\mathcal{L}_{\text{US-JEPA}} = \frac{1}{T} \sum_{i=1}^T \text{Smooth L1}(g_\phi(\mathbf{c}, p_i), \mathbf{y}_i) \quad (5)$$

By constraining both input and output to $\mathcal{P}_{\text{valid}}$, US-JEPA with USrc (USrc-JEPA) engineers the inputs to only model tissue texture and anatomical structure.

4.3. Training Pipeline

To facilitate standardization across our aggregated corpus of US frames, we implement a standardized preprocessing and sampling pipeline for training.

Preprocessing: Images are first converted to grayscale. Regions with minimal colored artifacts or annotations are inpainted as long as they occupy less than 5% of the total image area. To normalize for varying transducer gain settings across datasets, we perform intensity rescaling by mapping the 2nd and 98th percentiles of the pixel distribution to the full dynamic range. The USrc mask is used to condition the intensity rescaling only within the US content.

Data Balancing Strategy: A significant challenge in aggregating public medical datasets is the extreme variance in dataset size, which risks biasing the model toward the larger datasets. We mitigate this through a weighted dataset-level sampling strategy, where we define an upper bound, sampling threshold N_t of 50,000 to limit the effective size of each dataset for a training epoch. Thus, for each dataset D_i with an actual size $|D_i|$, the effective count is determined by $\min(|D_i|, N_t)$, and the probability $P(D_i)$ of drawing a sample from dataset D_i during training is then calculated as:

$$P(D_i) = \frac{\min(|D_i|, N_t)}{\sum_j \min(|D_j|, N_t)} \quad (6)$$

This strategy ensures that datasets larger than N_t contribute equally during training and smaller datasets contribute proportional to their true size. This approach balances maximizing data diversity and ensuring that the largest contributing datasets are not over represented.

4.4. US-JEPA Architecture

The context encoder (student) is a randomly initialized ViT-B/16 with an embedding dimension of 768. The predictor is a narrower transformer with an output embedding dimension of 384. The target encoder (teacher) is a frozen ViT-B/16 with the pretrained URFM weights. The predictor includes

a. Video and Volume		b. Static Frames	
Cardiac	$n_v: 23904$	Liver	$n_f: 191964$
Thyroid	$n_v: 17899$	Other	$n_f: 120564$
Prostate	$n_v: 1910$	Kidney	$n_f: 115237$
Liver	$n_v: 910$	Thyroid	$n_f: 110786$
Other	$n_v: 694$	Gallbladder	$n_f: 51682$
Lung	$n_v: 536$	Pancreas	$n_f: 34749$

Figure 2. Distribution of pretraining data. To characterize the dataset composition at the organ level, we report the distribution of a. temporal sequences, including videos and volumes (n_v), and b. individual static frames (n_f).

a linear adapter that projects its output from 384 to 768 to align with the target encoder’s feature space before the loss is computed. The detailed model and training configurations are provided in Appendix Section C.1.

5. Experiments

5.1. Data

5.1.1. PRETRAINING DATASET

Both US-JEPA and USrc-JEPA are developed with a large-scale, heterogeneous corpus of ultrasound data comprising 5,123,697 frames curated from 50 distinct publicly available datasets (Figure 2). To our knowledge, this is the largest aggregation of publicly available US datasets. The data contains three different US acquisition types with a majority (79.7%) of the frames derived from temporal video sequences and the remaining from volumetric (3D) scans or static 2D images. The dataset also spans a wide range of human anatomy, including major organ systems and important ancillary structures. Cardiac data represents the largest subset (23,904 videos), largely sourced from high-volume video datasets like EchoNet-Dynamic and EchoNet-LVH. This is complemented by significant representations of key organs, including the liver (318K frames), thyroid (264K frames) and prostate (227K frames), as well as breast (79K frames) and lung (55K). The data originates from a diverse array of clinical contexts, ranging from large-scale institutional repositories (ex. Stanford, TCIA, RadImageNet) to more specialized, curated datasets, providing the model with exposure to varying image qualities, transducer frequencies, and pathological presentations. Further details regarding the pretraining dataset are included in Appendix Section A.1.

Table 1. Summary of downstream datasets used for classification tasks, including the target organ, number of classes (Y), and total image counts. All datasets are public.

DATASET	ORGAN	TOTAL IMAGES
AUL (Y=3)	LIVER	735
BUSBRA (Y=2)	BREAST	1064
BUTTERFLY (Y=9)	MULTI-ORGAN	41076
FATTY LIV. (Y=2)	LIVER	550
GBCU (Y=3)	GALLBLADDER	1255
MMOTU (Y=8)	OVARY	1469
POCUS (Y=3)	LUNG	2064
TN5000 (Y=2)	THYROID	5000

5.1.2. ULTRABENCH DOWNSTREAM DATASET

To ensure standardized and reproducible evaluation, we leverage UltraBench (Tupper & Gagné), a publicly available benchmark encompassing diverse ultrasound tasks across segmentation, detection, and classification. We add implementation for BUSBRA and TN5000 to UltraBench to expand anatomical coverage for breast and thyroid. Our evaluation focuses on eight classification tasks, comprising both binary and multi-class endpoints (Table 2), to assess the discriminative ability and representation quality of our models. Five of the eight datasets focus primarily on cancer detection. FATTY LIVER and POCUS have non-oncological applications in fatty liver disease detection and lung pathology detection (healthy, pneumonia and COVID), respectively. Lastly, BUTTERFLY is a general multi-organ detection task. In Section 5.3 and Section 5.4, our figures specifically show results for these four datasets: FATTY LIVER and POCUS since they are non-cancer related, MMOTU since it is a challenging 8-class task and BUSBRA to demonstrate cancer-specific performance.

5.2. UltraBench Evaluation

To effectively evaluate the feature quality of US-JEPA and USrc-JEPA, we compare their performance against baselines using standard SSL practice of linear probing (Alain & Bengio, 2018). We identified six US foundation models with publicly available pretrained weights: USFM (Jiao et al., 2024), URFM (Kang et al., 2025), USF-MAE (Megahed et al., 2025), EchoCare (Zhang et al., 2025b), UltraSAM (Meyer et al., 2025), and SAMUS (Lin et al., 2024). UltraSAM and SAMUS are foundation models specifically developed for segmentation tasks, while the remaining are general ultrasound foundation models. Furthermore, we evaluate against two pretrained, state-of-the-art universal vision foundation models, DINOv3 and I-JEPA, which serve as out-of-domain benchmarks. Using the image encoder from each framework as a frozen feature extractor, we train linear probes for each downstream task across five random seeds to measure stability (Table 2).

The results demonstrate that US-JEPA and USrc-JEPA achieve state-of-the-art performance on five of the eight tasks (BUSBRA, FATTY LIVER, GBCU, MMOTU and POCUS), and fall in second-place on two of the remaining five tasks (AUL and TN5000). On the remaining task, BUTTERFLY, our framework underperforms the best baseline by less than 2% macro F1. Notably, our models excel in the most challenging scenarios where baseline methods struggle. The MMOTU dataset entails an eight-class ovarian tumor classification task. Average baseline performance drops below 40% on MMOTU, while US-JEPA establishes a new benchmark of 52.2%, surpassing the best baseline, URFM, by 9.5%. While URFM performs strongly on AUL and TN5000, our methods still offer competitive performance on the remaining downstream tasks, clearly beating general purpose vision models (DINOv3 and I-JEPA) and the majority of the domain-specific baselines.

5.3. Few-Shot Scaling for Linear Probe

To evaluate the efficiency and transferability of our models’ representations, we measure downstream performance with varying amounts of supervision. For each dataset, we train linear probes (across five seeds to measure stability) on every model’s frozen features using stratified subsets of the training data: 1%, 5%, 10%, 50%, 100%. By preserving the original UltraBench splits and class prevalence through subsampling, we quantify how effectively pretrained features affect learning in low-shot regimes. In this experiment, superior representation quality is evidenced by higher quantitative performance and faster performance convergence as label density decreases.

Figure 3 illustrates macro F1 performance across four datasets under varying label quantities for linear probing. We compare degradation against URFM and USFM. This pattern is most clearly seen with the FATTY LIVER downstream. When probes are trained with less than 10% of labels, our models achieve an average macro F1 of 18% higher than the URFM and USFM baselines. For the POCUS task, a similar trend is observed where the mean macro F1 degrades faster for the baselines compared to our models. As probes are trained with fewer labels, even for BUSBRA, MMOTU, and AUL (in Appendix Section D), our models are at least on par, if not better than URFM and USFM. Complete results for all downstream tasks are included in Appendix Section D.

5.4. Robustness to Domain-Specific Corruption

In real-world clinical environments, ultrasound image quality is frequently compromised by hardware constraints, operator variability, and suboptimal acquisition settings. To evaluate the stability of US-JEPA under such distribution shifts, we performed an incremental stress test consisting of

Table 2. **Linear probe on downstream datasets.** We compare results of linear probes trained using our proposed method against state-of-the-art baselines. We report the mean macro F1 score % over five seeds for all eight downstream datasets. Bold indicates the best result and underlining indicates the second best.

MODEL	AUL	BUSBRA	BUTTERFLY	FATTY LIV.	GBCU	MMOTU	POCUS	TN5000
DINOv3	64.3±0.6	70.9±1.7	91.7±0.4	55.8±5.5	61.7±0.5	37.2±0.6	91.4±0.4	67.5±0.4
I-JEPA	61.5±1.1	71.2±4.0	90.5±0.6	54.8±1.6	53.7±0.4	35.3±0.6	88.1±0.4	68.9±0.2
ULTRASAM	62.6±3.1	70.2±3.1	89.6±2.4	66.9±3.3	43.5±4.9	39.7±1.8	87.3±2.1	63.9±2.0
SAMUS	40.2±0.9	65.9±0.3	91.5±0.0	42.1±0.0	48.8±0.3	20.4±0.2	76.2±0.1	51.7±0.0
ECHOCARE	49.2±2.4	64.4±0.0	84.1±0.7	42.1±0.0	36.2±0.5	21.1±0.1	73.8±3.9	49.8±3.8
USF-MAE	58.1±1.4	62.9±0.5	91.1±0.3	42.1±0.0	45.9±0.3	28.7±0.3	90.1±0.0	56.3±1.1
USFM	61.6±1.2	<u>74.6±0.5</u>	92.4±0.3	73.6±8.8	<u>67.4±0.6</u>	33.8±0.3	85.7±0.5	65.0±2.6
URFM	71.5±1.1	69.5±2.2	<u>92.1±0.4</u>	<u>82.6±6.0</u>	<u>59.1±1.7</u>	42.7±0.4	91.7±0.3	77.4±0.4
US-JEPA	<u>69.6±1.5</u>	73.8±1.1	90.8±0.3	82.5±1.1	67.0±1.4	52.2±0.2	93.1±0.0	<u>73.1±0.7</u>
USrc-JEPA	67.6±0.5	76.0±1.2	91.5±0.6	89.2±0.9	70.2±0.5	<u>46.8±0.2</u>	<u>92.5±0.1</u>	70.8±1.3

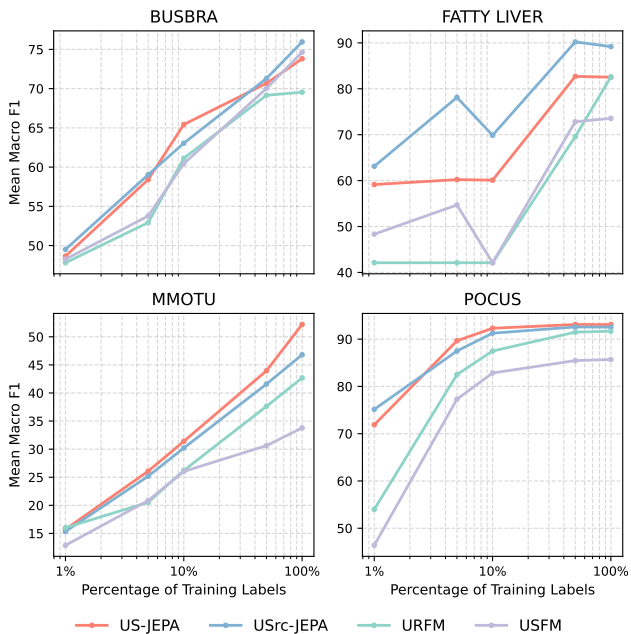


Figure 3. **Results for few-shot scaling.** We report the mean macro F1 score % over five seeds for each model’s probe to measure performance with 1% to 100% of training labels. Note: each dataset is plotted on a unique y-axis scale to better highlight model-specific performance trends.

three synthetic, domain-specific image corruptions: Gaussian blur, contrast depletion, and correlated speckle noise.

For each corruption type, we evaluate downstream performance on test sets across three levels of increasing severity ($\epsilon \in \{1, 2, 3\}$). While blur and contrast are implemented via standard intensity transforms, we model speckle as a multiplicative, spatially-correlated process to approximate the “grainy” texture inherent to ultrasound scans. More detailed implementations for these corruptions are provided in Appendix Section E.2.

Figure 4 visualizes the performance degradation for a subset of downstream tasks, with the remaining tasks detailed in Appendix Section E.1. Most notably, both US-JEPA and USrc-JEPA demonstrate significant resilience to the blur corruption. On the POCUS dataset, URFM degrades to nearly half of its uncorrupted performance, dropping from 91.7 to 46.8 F1 at maximum blur severity. In contrast, US-JEPA and USrc-JEPA are much more resilient, with F1 only dropping to 69.5 and 78.4 respectively, at maximum blur severity. Similarly, on the BUTTERFLY dataset (Appendix Section E.1), URFM drops to 22.4 F1 under severe blur, while US-JEPA and USrc-JEPA maintain F1 performance at 80.8 and 70.9. In these severe blur cases, the second baseline USFM drops to 77.8 and 59.8 F1 for POCUS and BUTTERFLY, exhibiting less degradation than URFM but still performs worse than both our models for BUTTERFLY.

Regarding texture and intensity corruptions, our models match or exceed URFM and USFM for most downstream tasks. The main pitfall can be seen with GBCU and TN5000 (Appendix Section E.1). On GBCU, URFM maintains consistent performance with F1 only decreasing by 8.9% from normal to the highest contrast severity, while our models drop by 47%. A similar pattern is seen on TN5000, where URFM drops by 11% while US-JEPA and USrc-JEPA drop by 23.2% and 17.7%, respectively. This performance disparity likely stems from a difference in gallbladder and thyroid pretraining data density. While our dataset is larger overall, gallbladder and thyroid frames constitute only 0.27% and 5.2% of our data, respectively, compared to 4% and 44.2% in the smaller URFM pretraining set. This difference in prevalence may have limited our model’s ability to learn stronger features for these anatomies. In other cases, URFM, USFM and our models maintain comparable performance, showing expected degradation under increasingly severe contrast reduction.

For speckle corruption, our models demonstrate remarkable stability. Specifically on BUTTERFLY, US-JEPA and USrc-

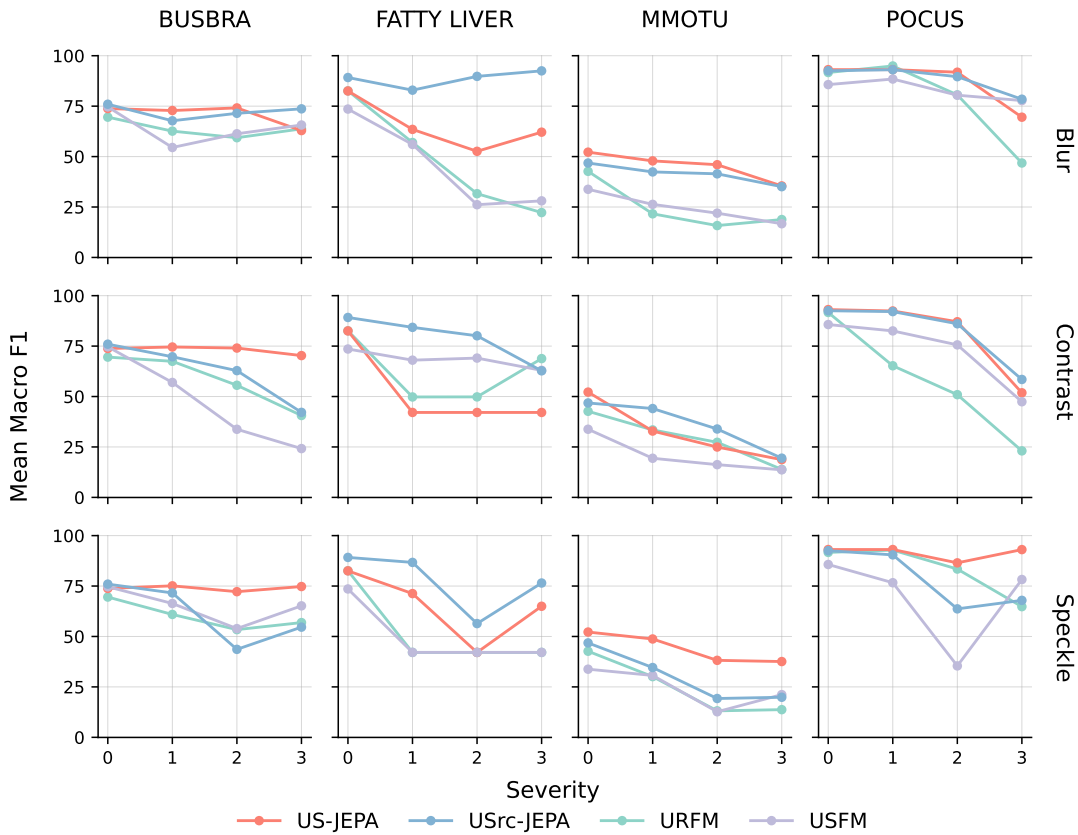


Figure 4. **Robustness to domain-specific corruption.** Results show the mean macro F1 across five seeds for each model-dataset-corruption permutation. Linear probes were trained on full, uncorrupted training sets and evaluated on increasingly corrupted test sets to assess structural representation stability.

JEPA only drop by 0.6% and 9.8% under severe speckle noise ($\epsilon = 3$), whereas USFM and URFM drop by 25% and 44.6%. Notably, across all downstream tasks, US-JEPA and USrc-JEPA outperform or match URFM under peak speckle severity, demonstrating superior robustness to this prevalent ultrasound-specific noise. US-JEPA also consistently outperforms USFM at the highest speckle severity across all eight downstreams. While USFM shows competitive results against USrc-JEPA on four benchmarks, it remains inferior to USrc-JEPA on the remaining half, often by substantial margins, reaching a performance gap of up to 34.39% on FATTY LIVER.

Ultimately, this stress test quantifies the invariance of our learned representations under significant corruption relative to the current state-of-the-art, URFM and additional baseline, USFM. By evaluating against domain-specific synthetic noise, we provide a practical validation of US-JEPA and USrc-JEPA’s feature stability. This evaluation is a critical requirement given the high variance in US image quality across different manufacturers, operators, and clinical en-

vironments. The observed performance under corruption suggests that our approach is able to better capture structural semantics in US instead of overfitting to superficial, pixel-level features.

6. Discussion

We present US-JEPA, a novel approach that demonstrates that training using a JEPA framework with a robust, static teacher yields stable, data-efficient representations for ultrasound. By adopting the SALT paradigm, we decouple the optimization of the student and teacher and leverage the semantic priors of a domain-specific teacher. Furthermore, with USrc-JEPA we show that adding USrc to the framework also achieves competitive performance on downstream tasks. This efficiency is highlighted in our downstream stress tests: US-JEPA remains robust in low-data regimes for linear probing and maintains performance during out-of-distribution evaluation through domain-specific corruptions. Despite these successes, certain limitations remain. The modest performance in specific corruption experiments and

on downstream datasets like TN5000 and AUL suggests that performance may be sensitive to organ-level density in pretraining data. Moving forward, we will build a more diverse pretraining corpus and implement an organ-weighted sampling strategy to improve downstream results.

This work also advances standardization in ultrasound foundation model research through three key contributions. First, we provide the first rigorous linear probing comparison across all published models to assess intrinsic representation quality. Second, we expand the UltraBench framework by integrating the TN5000 and BUSBRA classification tasks for broader anatomical coverage. Finally, we establish baseline performance for existing models using UltraBench, creating a better foundation to benchmark comparative performance moving forward.

These findings confirm the utility of the JEPA framework for ultrasound self-supervised learning and position US-JEPA as a clinically impactful ultrasound foundation model.

Impact Statement

US-JEPA is a novel paradigm for applying self-supervised learning to the US image domain. By pretraining on the largest publicly available corpus of US imaging, we demonstrate competitive results with previous US foundation models. We establish the importance of few-shot scaling for linear probes and evaluating robustness to domain-specific corruptions to truly determine representation quality in US. Most importantly, we standardize comparative benchmarking by evaluating all current US foundation models on eight tasks from UltraBench. By relying exclusively on publicly accessible data and standardized evaluation, US-JEPA lowers the barrier to entry for US research, fostering broader participation and more equitable development of ultrasound foundation models.

References

- Abbasian Ardakani, A., Mohammadi, A., Mirza-Aghazadeh-Attari, M., and Acharya, U. R. An open-access breast lesion ultrasound image database: Applicable in artificial intelligence studies. *Computers in Biology and Medicine*, 152:106438, January 2023. ISSN 0010-4825. doi: 10.1016/j.compbiomed.2022.106438. URL <https://www.sciencedirect.com/science/article/pii/S0010482522011465>.
- Agata Momot. Common Carotid Artery Ultrasound Images, November 2022. URL <https://data.mendeley.com/datasets/d4xt63mgjm/1>.
- Al-Dhabyani, W., Gomaa, M., Khaled, H., and Fahmy, A. Dataset of breast ultrasound images. *Data in Brief*, 28: 104863, November 2019. ISSN 2352-3409. doi: 10.1016/j.dib.2019.104863. URL <https://pmc.ncbi.nlm.nih.gov/articles/PMC6906728/>.
- Alain, G. and Bengio, Y. Understanding intermediate layers using linear classifier probes, November 2018. URL <http://arxiv.org/abs/1610.01644>. arXiv:1610.01644 [stat].
- Ambdsdorf, J., Munk, A., Llambias, S., Christensen, A. N., Mikolaj, K., Balestrieri, R., Tolsgaard, M., Feragen, A., and Nielsen, M. General Methods Make Great Domain-specific Foundation Models: A Case-study on Fetal Ultrasound, June 2025. URL <http://arxiv.org/abs/2506.19552>. arXiv:2506.19552 [cs].
- Assran, M., Duval, Q., Misra, I., Bojanowski, P., Vincent, P., Rabbat, M., LeCun, Y., and Ballas, N. Self-Supervised Learning from Images with a Joint-Embedding Predictive Architecture, April 2023. URL <http://arxiv.org/abs/2301.08243>. arXiv:2301.08243 [cs].
- Basu, S., Gupta, M., Rana, P., Gupta, P., and Arora, C. Surpassing the Human Accuracy: Detecting Gallbladder Cancer from USG Images with Curriculum Learning. In *2022 IEEE/CVF Conference on Computer Vision and Pattern Recognition (CVPR)*, pp. 20854–20864. IEEE, 6 2022. ISBN 978-1-6654-6946-3. doi: 10.1109/CVPR52688.2022.02022.
- Baum, Z. M. C., Shaheer U. Saeed, Min, Z., Yipeng Hu, and Barratt, D. C. MR to Ultrasound Registration for Prostate Challenge - Dataset, June 2023. URL <https://zenodo.org/record/8004388>.
- Born, J., Wiedemann, N., Cossio, M., Buhre, C., Brändle, G., Leidermann, K., Goulet, J., Aujayeb, A., Moor, M., Rieck, B., and Borgwardt, K. Accelerating Detection of Lung Pathologies with Explainable Ultrasound Image Analysis. *Applied Sciences*, 11(2):672, 1 2021. ISSN 2076-3417. doi: 10.3390/app11020672.
- Borna, M.-R., Saadat, H., Sepehri, M. M., Torkashvand, H., Torkashvand, L., and Pilehvari, S. AI-powered diagnosis of ovarian conditions: insights from a newly introduced ultrasound dataset. *Frontiers in Physiology*, 16, July 2025. ISSN 1664-042X. doi: 10.3389/fphys.2025.1520898. URL <https://www.frontiersin.org/journals/physiology/articles/10.3389/fphys.2025.1520898/full>. Publisher: Frontiers.
- Butterfly Network. Butterflynetwork/mitgrandhack2018. <https://github.com/ButterflyNetwork/MITGrandHack2018>, 2018. GitHub repository, accessed 2018.

- Byra, M., Styczynski, G., Szmigielski, C., Kalinowski, P., Michałowski, Ł., Paluszkiwicz, R., Ziarkiewicz-Wróblewska, B., Zieniewicz, K., Sobieraj, P., and Nowicki, A. Transfer learning with deep convolutional neural network for liver steatosis assessment in ultrasound images. *International Journal of Computer Assisted Radiology and Surgery*, 13(12):1895–1903, 12 2018. ISSN 1861-6410. doi: 10.1007/s11548-018-1843-2.
- Caron, M., Touvron, H., Misra, I., Jégou, H., Mairal, J., Bojanowski, P., and Joulin, A. Emerging Properties in Self-Supervised Vision Transformers, May 2021. URL <http://arxiv.org/abs/2104.14294>. arXiv:2104.14294 [cs].
- Chen, T., Kornblith, S., Norouzi, M., and Hinton, G. A Simple Framework for Contrastive Learning of Visual Representations, July 2020. URL <http://arxiv.org/abs/2002.05709>. arXiv:2002.05709 [cs].
- Choudhari, A. and Korde, A. PCOS detection using ultrasound images. URL <https://www.kaggle.com/datasets/anaghachoudhari/pcos-detection-using-ultrasound-images>.
- Ding, Y., Yang, Q., Wang, Y., Chen, D., Qin, Z., and Zhang, J. MallesNet: A multi-object assistance based network for brachial plexus segmentation in ultrasound images. *Medical Image Analysis*, 80:102511, August 2022. ISSN 1361-8415. doi: 10.1016/j.media.2022.102511. URL <https://www.sciencedirect.com/science/article/pii/S136184152200158X>.
- Duffy, G., Cheng, P. P., Yuan, N., He, B., Kwan, A. C., Shun-Shin, M. J., Alexander, K. M., Ebinger, J., Lungren, M. P., Rader, F., Liang, D. H., Schnittger, I., Ashley, E. A., Zou, J. Y., Patel, J., Witteles, R., Cheng, S., and Ouyang, D. High-Throughput Precision Phenotyping of Left Ventricular Hypertrophy With Cardiovascular Deep Learning. *JAMA Cardiology*, 7(4):386–395, April 2022. ISSN 2380-6583. doi: 10.1001/jamacardio.2021.6059. URL <https://doi.org/10.1001/jamacardio.2021.6059>.
- Ebadi, A., Xi, P., MacLean, A., Florea, A., Tremblay, S., Kohli, S., and Wong, A. COVIDx-US: An Open-Access Benchmark Dataset of Ultrasound Imaging Data for AI-Driven COVID-19 Analytics. *Frontiers in Bioscience*, 27(7):198, June 2022. ISSN 2768-6698. doi: 10.31083/j.fbl2707198. Place: Landmark edition.
- Eisenbrey, J., Lyschik, A., and Wessner, C. Ultrasound data of a variety of liver masses, 2021. URL <https://www.cancerimagingarchive.net/collection/b-mode-and-ceus-liver/>.
- Geng, Y., Meng, G., Chen, M., Cao, G., Zhao, M., Zhao, J., and Liu, H. Force Sensing Guided Artery-Vein Segmentation via Sequential Ultrasound Images. In Linguraru, M. G., Dou, Q., Feragen, A., Giannarou, S., Glocker, B., Lekadir, K., and Schnabel, J. A. (eds.), *Medical Image Computing and Computer Assisted Intervention – MICCAI 2024*, pp. 656–666, Cham, 2024. Springer Nature Switzerland. ISBN 978-3-031-72083-3. doi: 10.1007/978-3-031-72083-3_61.
- Gómez-Flores, W., Gregorio-Calas, M. J., and Coelho de Albuquerque Pereira, W. BUS-BRA: A breast ultrasound dataset for assessing computer-aided diagnosis systems. *Medical Physics*, 51(4):3110–3123, 4 2024. ISSN 0094-2405. doi: 10.1002/mp.16812.
- gong, h. haifangong/TRFE-Net-for-thyroid-nodule-segmentation, February 2026. URL <https://github.com/haifangong/TRFE-Net-for-thyroid-nodule-segmentation>. original-date: 2021-02-11T08:33:39Z.
- Guo, Y., Duan, X., Wang, C., and Guo, H. Segmentation and recognition of breast ultrasound images based on an expanded U-Net. *PLoS ONE*, 16(6):e0253202, June 2021. ISSN 1932-6203. doi: 10.1371/journal.pone.0253202. URL <https://pmc.ncbi.nlm.nih.gov/articles/PMC8205136/>.
- Hann, A., Bettac, L., Haenle, M. M., Graeter, T., Berger, A. W., Dreyhaupt, J., Schmalstieg, D., Zoller, W. G., and Egger, J. Algorithm guided outlining of 105 pancreatic cancer liver metastases in Ultrasound. *Scientific Reports*, 7(1):12779, October 2017. ISSN 2045-2322. doi: 10.1038/s41598-017-12925-z. URL <https://www.nature.com/articles/s41598-017-12925-z>. Publisher: Nature Publishing Group.
- He, K., Fan, H., Wu, Y., Xie, S., and Girshick, R. Momentum Contrast for Unsupervised Visual Representation Learning, March 2020. URL <http://arxiv.org/abs/1911.05722>. arXiv:1911.05722 [cs].
- He, Q., Bano, S., Liu, J., Liu, W., Stoyanov, D., and Zuo, S. Query2<math><msup is="true"><mrow is="true"></mrow><mrow is="true"></mrow></msup></math>: Query over queries for improving gastrointestinal stromal tumour detection in an endoscopic ultrasound. *Computers in Biology and Medicine*, 152:106424, January 2023. ISSN 0010-4825. doi: 10.1016/j.combiomed.2022.106424. URL <https://www.sciencedirect.com/science/article/pii/S0010482522011325>.

- Hondru, V., Croitoru, F. A., Minaee, S., Ionescu, R. T., and Sebe, N. Masked Image Modeling: A Survey, July 2025. URL <http://arxiv.org/abs/2408.06687>. arXiv:2408.06687 [cs].
- Hou, X., Hua, M., Zhang, W., Ji, J., Zhang, X., Jiang, H., Li, M., Wu, X., Zhao, W., Sun, S., Cao, L., and Wang, L. An ultrasonography of thyroid nodules dataset with pathological diagnosis annotation for deep learning. *Scientific Data*, 11(1):1272, November 2024. ISSN 2052-4463. doi: 10.1038/s41597-024-04156-5. URL <https://www.nature.com/articles/s41597-024-04156-5>. Publisher: Nature Publishing Group.
- Huang, J., Zhang, J., Zhang, Y., Li, X., Ma, X., Deng, J., Shen, H., Wang, D., mei, I., and Lei, C. BUSI_wlu: Breast Cancer Ultrasound Image Dataset, October 2023. URL <https://data.mendeley.com/datasets/k6cpmwybk3/1>.
- Iqbal, A. BUS_uc. 1, October 2023a. doi: 10.17632/3ksd7w7jxk.1. URL <https://data.mendeley.com/datasets/3ksd7w7jxk/1>. Publisher: Mendeley Data.
- Iqbal, A. BUSC Dataset. 1, March 2023b. doi: 10.17632/vckdnhtw26.1. URL <https://data.mendeley.com/datasets/vckdnhtw26/1>. Publisher: Mendeley Data.
- Jiao, J., Zhou, J., Li, X., Xia, M., Huang, Y., Huang, L., Wang, N., Zhang, X., Zhou, S., Wang, Y., and Guo, Y. USFM: A universal ultrasound foundation model generalized to tasks and organs towards label efficient image analysis. *Medical Image Analysis*, 96:103202, August 2024. ISSN 1361-8415. doi: 10.1016/j.media.2024.103202. URL <https://www.sciencedirect.com/science/article/pii/S1361841524001270>.
- Jimenez, Y., Rodriguez-Alvarez, M. J., Escudero, L., Sandoval, C., and Lakshminarayanan, V. Ultrasound Breast images denoising using Generative Adversarial Networks (GANs), 2024. URL <https://data.mendeley.com/datasets/g3cmj46xyx/1>.
- Juvekar, P., Dorent, R., Kögl, F., Torio, E., Barr, C., Rigolo, L., Galvin, C., Jowkar, N., Kazi, A., Haouchine, N., Cheema, H., Navab, N., Pieper, S., Wells, W. M., Bi, W. L., Golby, A., Frisken, S., and Kapur, T. The Brain Resection Multimodal Imaging Database (ReMIND), 2023. URL <https://www.cancerimagingarchive.net/collection/remind/>.
- Kang, Q., Gao, J., Zhao, H., He, Z., Li, K., and Lao, Q. D2MAE: Diffusional Deblurring MAE for Ultrasound Image Pre-training. Kang, Q., Lao, Q., Gao, J., Bao, W., He, Z., Du, C., Lu, Q., and Li, K. URFM: A general Ultrasound Representation Foundation Model for advancing ultrasound image diagnosis. *iScience*, 28(8), August 2025. ISSN 2589-0042. doi: 10.1016/j.isci.2025.112917. URL [https://www.cell.com/iscience/abstract/S2589-0042\(25\)01178-2](https://www.cell.com/iscience/abstract/S2589-0042(25)01178-2). Publisher: Elsevier.
- Kim, S., Jin, P., Song, S., Chen, C., Li, Y., Ren, H., Li, X., Liu, T., and Li, Q. EchoFM: Foundation Model for Generalizable Echocardiogram Analysis. *IEEE transactions on medical imaging*, 44(10):4049–4062, October 2025. ISSN 0278-0062. doi: 10.1109/TMI.2025.3580713. URL <https://pmc.ncbi.nlm.nih.gov/articles/PMC12616925/>.
- Kim-Ann. ftsvd/USAnotAI, June 2024. URL <https://github.com/ftsvd/USAnotAI>. original-date: 2019-07-26T17:37:10Z.
- Kirillov, A., Mintun, E., Ravi, N., Mao, H., Rolland, C., Gustafson, L., Xiao, T., Whitehead, S., Berg, A. C., Lo, W.-Y., Dollár, P., and Girshick, R. Segment Anything, April 2023. URL <http://arxiv.org/abs/2304.02643>. arXiv:2304.02643 [cs].
- Krönke, M., Eilers, C., Dimova, D., Köhler, M., Buschner, G., Schweiger, L., Konstantinidou, L., Makowski, M., Nagarajah, J., Navab, N., Weber, W., and Wendler, T. Tracked 3D ultrasound and deep neural network-based thyroid segmentation reduce interobserver variability in thyroid volumetry. *PLOS ONE*, 17(7):e0268550, July 2022. ISSN 1932-6203. doi: 10.1371/journal.pone.0268550. URL <https://dx.plos.org/10.1371/journal.pone.0268550>.
- Leclerc, S., Smistad, E., Pedrosa, J., Østvik, A., Cervenansky, F., Espinosa, F., Espeland, T., Berg, E. A. R., Jodoin, P.-M., Grenier, T., Lartizien, C., D’hooge, J., Lovstakken, L., and Bernard, O. Deep Learning for Segmentation Using an Open Large-Scale Dataset in 2D Echocardiography. *IEEE Transactions on Medical Imaging*, 38(9):2198–2210, September 2019. ISSN 1558-254X. doi: 10.1109/TMI.2019.2900516. URL <https://ieeexplore.ieee.org/document/8649738>.
- Li, J., Zhang, P., Wang, T., Wang, K., and Sheng, B. LEPset, June 2023. URL <https://zenodo.org/record/8041285>.
- Li, X., Huang, C., Li, C.-L., Malach, E., Susskind, J., Thilak, V., and Littwin, E. Rethinking JEPA: Compute-Efficient Video SSL with Frozen Teachers, September 2025. URL <http://arxiv.org/abs/2509.24317>. arXiv:2509.24317 [cs].

- Liang, X., Cao, Q., Huang, R., and Lin, L. Recognizing focal liver lesions in contrast-enhanced ultrasound with discriminatively trained spatio-temporal model. In *2014 IEEE 11th International Symposium on Biomedical Imaging (ISBI)*, pp. 1184–1187, Beijing, China, April 2014. IEEE. ISBN 978-1-4673-1961-4. doi: 10.1109/ISBI.2014.6868087. URL <http://ieeexplore.ieee.org/document/6868087/>.
- Lin, X., Xiang, Y., Yu, L., and Yan, Z. Beyond Adapting SAM: Towards End-to-End Ultrasound Image Segmentation via Auto Prompting. In Linguraru, M. G., Dou, Q., Feragen, A., Giannarou, S., Glocker, B., Lekadir, K., and Schnabel, J. A. (eds.), *Medical Image Computing and Computer Assisted Intervention – MICCAI 2024*, volume 15008, pp. 24–34. Springer Nature Switzerland, Cham, 2024. ISBN 978-3-031-72110-6 978-3-031-72111-3. doi: 10.1007/978-3-031-72111-3_3. URL https://link.springer.com/10.1007/978-3-031-72111-3_3. Series Title: Lecture Notes in Computer Science.
- Lin, Z., Lin, J., Zhu, L., Fu, H., Qin, J., and Wang, L. A New Dataset and A Baseline Model for Breast Lesion Detection in Ultrasound Videos, July 2022. URL <http://arxiv.org/abs/2207.00141>. arXiv:2207.00141 [eess].
- Luo, G., Xu, M., Chen, H., Liang, X., Tao, X., Ni, D., Jeong, H., Kim, C., Stock, R., Baumgartner, M., Kirchhoff, Y., Rokuss, M., Maier-Hein, K., Yang, Z., Fan, T., Boutry, N., Tereshchenko, D., Moine, A., Charmentant, M., Sauer, J., Du, H., Bai, X.-H., Raikar, V. P., Montoya-del Angel, R., Marti, R., Luna, M., Lee, D., Qayyum, A., Mazher, M., Guo, Q., Wang, C., Awasthi, N., Zhao, Q., Wang, W., Wang, K., Wang, Q., and Dong, S. Tumor Detection, Segmentation and Classification Challenge on Automated 3D Breast Ultrasound: The TDSC-ABUS Challenge, January 2025. URL <http://arxiv.org/abs/2501.15588>. arXiv:2501.15588 [eess].
- Megahed, Y., Ducharme, R., Erman, A., Walker, M., Hawken, S., and Chan, A. D. C. USF-MAE: Ultrasound Self-Supervised Foundation Model with Masked Autoencoding, November 2025. URL <http://arxiv.org/abs/2510.22990>. arXiv:2510.22990 [eess].
- Mei, X., Liu, Z., Robson, P. M., Marinelli, B., Huang, M., Doshi, A., Jacobi, A., Cao, C., Link, K. E., Yang, T., Wang, Y., Greenspan, H., Deyer, T., Fayad, Z. A., and Yang, Y. RadImageNet: An Open Radiologic Deep Learning Research Dataset for Effective Transfer Learning. *Radiology: Artificial Intelligence*, 4(5): e210315, September 2022. doi: 10.1148/ryai.210315. URL <https://pubs.rsna.org/doi/10.1148/ryai.210315>. Publisher: Radiological Society of North America.
- Meiburger, K. DATASET for "Deep learning segmentation of transverse musculoskeletal ultrasound images for neuromuscular disease assessment", July 2021. URL <https://data.mendeley.com/datasets/3jy kz7wz8d/1>.
- Meiburger, K. DATASET for: "Carotid Ultrasound Boundary Study (CUBS): Technical considerations on an open multi-center analysis of computerized measurement systems for intima-media thickness measurement on common carotid artery longitudinal B-mode ultrasound scans", March 2022. URL <https://data.mendeley.com/datasets/m7ndn58sv6/1>.
- Meyer, A., Murali, A., Zarin, F., Mutter, D., and Padoy, N. Ultrasam: a foundation model for ultrasound using large open-access segmentation datasets. *International Journal of Computer Assisted Radiology and Surgery*, September 2025. ISSN 1861-6429. doi: 10.1007/s11548-025-03517-8. URL <https://doi.org/10.1007/s11548-025-03517-8>.
- Montoya, A., Sterling, D., Hasnin, kaggle446, shirzad, Cukierski, W., and yffud. Ultrasound nerve segmentation. <https://kaggle.com/competitions/ultrasound-nerve-segmentation>, 2016. Kaggle.
- Natarajan, S., Priester, A., Margolis, D., Huang, J., and Marks, L. Prostate MRI and Ultrasound With Pathology and Coordinates of Tracked Biopsy (Prostate-MRI-US-Biopsy), 2020. URL <https://www.cancerimagingarchive.net/collection/prostate-mri-us-biopsy/>.
- Ndzimbong, W., Fourniol, C., Themyr, L., Thome, N., Keeza, Y., Sauer, B., Piéchaud, P.-T., Méjean, A., Marescaux, J., George, D., Mutter, D., Hostettler, A., and Collins, T. TRUSTED: The Paired 3D Transabdominal Ultrasound and CT Human Data for Kidney Segmentation and Registration Research. *Scientific Data*, 12(1):615, April 2025. ISSN 2052-4463. doi: 10.1038/s41597-025-04467-1. URL <https://www.nature.com/articles/s41597-025-04467-1>. Publisher: Nature Publishing Group.
- Oquab, M., Darcet, T., Moutakanni, T., Vo, H., Szafraniec, M., Khalidov, V., Fernandez, P., Haziza, D., Massa, F., El-Nouby, A., Assran, M., Ballas, N., Galuba, W., Howes, R., Huang, P.-Y., Li, S.-W., Misra, I., Rabbat, M., Sharma, V., Synnaeve, G., Xu, H., Jegou, H., Mairal, J., Labatut, P., Joulin, A., and Bojanowski, P. DINOv2: Learning Robust Visual Features without Supervision, Febru-

- Yang, J., Ding, X., Zheng, Z., Xu, X., and Li, X. GraphEcho: Graph-Driven Unsupervised Domain Adaptation for Echocardiogram Video Segmentation, September 2023. URL <http://arxiv.org/abs/2309.11145>. arXiv:2309.11145 [cs].
- Yap, M. H., Pons, G., Martí, J., Ganau, S., Sentís, M., Zwiggelaar, R., Davison, A. K., and Martí, R. Automated Breast Ultrasound Lesions Detection Using Convolutional Neural Networks. *IEEE Journal of Biomedical and Health Informatics*, 22(4):1218–1226, July 2018. ISSN 2168-2194, 2168-2208. doi: 10.1109/JBHI.2017.2731873. URL <https://ieeexplore.ieee.org/document/8003418/>.
- Zhang, H., Liu, Q., Han, X., Niu, L., and Sun, W. TN5000: An Ultrasound Image Dataset for Thyroid Nodule Detection and Classification. *Scientific Data*, 12(1):1437, 8 2025a. ISSN 2052-4463. doi: 10.1038/s41597-025-05757-4.
- Zhang, H., Wu, Y., Zhao, M., Chen, Z., Li, R., Zhu, F., Zhao, H., Yuan, X., Yang, M., Qiu, C., Cong, X., Chen, H., Luan, L., Wong, R. H. L., Liao, H., Graham, C. A., Chang, S., Tao, G., Yi, D., Lei, Z., Navab, N., Ourselin, S., Luo, J., Liu, H., and Meng, G. A Fully Open and Generalizable Foundation Model for Ultrasound Clinical Applications, September 2025b. URL <http://arxiv.org/abs/2509.11752>. arXiv:2509.11752 [cs].
- Zhang, S., Xu, Y., Usuyama, N., Xu, H., Bagga, J., Tinn, R., Preston, S., Rao, R., Wei, M., Valluri, N., Wong, C., Tupini, A., Wang, Y., Mazzola, M., Shukla, S., Liden, L., Gao, J., Crabtree, A., Piening, B., Bifulco, C., Lungren, M. P., Naumann, T., Wang, S., and Poon, H. A Multimodal Biomedical Foundation Model Trained from Fifteen Million Image–Text Pairs. *NEJM AI*, 2(1):AIoa2400640, January 2025c. doi: 10.1056/AIoa2400640. URL <https://ai.nejm.org/doi/full/10.1056/AIoa2400640>. Publisher: Massachusetts Medical Society.
- Zhao, Q., Lyu, S., Bai, W., Cai, L., Liu, B., Cheng, G., Wu, M., Sang, X., Yang, M., and Chen, L. Mmotu: A multi-modality ovarian tumor ultrasound image dataset for unsupervised cross-domain semantic segmentation, 2023. URL <https://arxiv.org/abs/2207.06799>.

A. Dataset Details

A.1. Pretraining Datasets

For complete transparency, we have included the name of each data set and associated metadata.

Table 3. Comprehensive breakdown of datasets used, categorized by anatomical region, frame type, and total frame count.

DATASET NAME	ANATOMY	FRAME TYPE	FRAME COUNT
ULTRASOUNDCASES.INFO	ABDOMINAL	STATIC	3199
ABDOMINAL_US (VITALE ET AL., 2020)	ABDOMINAL	STATIC	617
ULTRASOUNDCASES.INFO	APPENDIX	STATIC	781
ULTRASOUNDCASES.INFO	BLADDER	STATIC	450
USANOTAI (KIM-ANN, 2024)	BLADDER	STATIC	61
RADIMAGENET (MEI ET AL., 2022)	BLADDER	STATIC	758
USANOTAI	BOWEL	STATIC	61
ULTRASOUNDCASES.INFO	BRAIN	STATIC	466
REMIND (JUVEKAR ET AL., 2023)	BRAIN	VIDEO	18734
ULTRASOUNDCASES.INFO	BREAST	STATIC	4956
BUSI (AL-DHABYANI ET AL., 2019)	BREAST	STATIC	780
BUS_UC (IQBAL, 2023A)	BREAST	STATIC	811
BREAST-LESIONS-USG (PAWŁOWSKA ET AL., 2024)	BREAST	STATIC	256
BUSC (IQBAL, 2023B)	BREAST	STATIC	250
DATASETA (JIMENEZ ET AL., 2024)	BREAST	STATIC	250
BUV (LIN ET AL., 2022)	BREAST	VIDEO	25026
BUID (ABBASIAN ARDAKANI ET AL., 2023)	BREAST	STATIC	205
ABUS-TDSC (LUO ET AL., 2025)	BREAST	VOLUME	44474
BREAST.S1 (GUO ET AL., 2021)	BREAST	STATIC	201
UDIAT (YAP ET AL., 2018)	BREAST	STATIC	163
BUSI.WHU (HUANG ET AL., 2023)	BREAST	STATIC	927
BUS_UCLM (VALLEZ ET AL., 2024)	BREAST	STATIC	683
CARDIACCAUS (AGATA MOMOT, 2022)	CARDIAC	STATIC	1100
ULTRASOUNDCASES.INFO	CARDIAC	STATIC	1443
ECHONET-LVH (DUFFY ET AL., 2022)	CARDIAC	VIDEO	1957928
CAROTID US BOUNDARY STUDY (MEIBURGER, 2022)	CARDIAC	STATIC	500
CAMUS (LECLERC ET AL., 2019)	CARDIAC	VIDEO	19232
CARDIACUDC (YANG ET AL., 2023)	CARDIAC	VIDEO	38071
ECHONET: TEE-VIEW-CLASSIFIER (STEFFNER ET AL., 2024)	CARDIAC	VIDEO	55261
ECHONET DYNAMIC (OUYANG ET AL.)	CARDIAC	VIDEO	1770636
RADIMAGENET	CARDIAC	STATIC	19062
RADIMAGENET	FIBROID	STATIC	2095
GB1 (TURKI ET AL., 2025)	GALLBLADDER	STATIC	10692
USANOTAI	GALLBLADDER	STATIC	61
RADIMAGENET	GALLBLADDER	STATIC	39743
ULTRASOUNDCASES.INFO	GALLBLADDER	STATIC	1186
GIST_EUS (HE ET AL., 2023)	GASTROINTESTINAL	STATIC	514
ULTRASOUNDCASES.INFO	GASTROINTESTINAL	STATIC	2618
USANOTAI	KIDNEY	STATIC	61
TRUSTED (NDZIMBONG ET AL., 2025)	KIDNEY	VOLUME	7280
OPENKIDNEY (SINGLA ET AL., 2022)	KIDNEY	STATIC	500
RADIMAGENET	KIDNEY	STATIC	111252
ULTRASOUNDCASES.INFO	KIDNEY	STATIC	3924
RADIMAGENET	LIVER	STATIC	78535
ULTRASOUNDCASES.INFO	LIVER	STATIC	2714
USANOTAI	LIVER	STATIC	61
SYSU-CEUS-FLL (LIANG ET AL., 2014)	LIVER	SAMPLED VIDEO	110654
B-MODE-AND-CEUS-LIVER (EISENBREY ET AL., 2021)	LIVER	VIDEO	126543
COVID-BLUES (BORN ET AL., 2021)	LUNG	VIDEO	31696
COVIDx-US (EBADI ET AL., 2022)	LUNG	VIDEO	22697
ULTRASOUNDCASES.INFO	LUNG	STATIC	714
ULTRASOUNDCASES.INFO	LYMPH NODE	STATIC	320
ULTRASOUNDCASES.INFO	MUSCLE	STATIC	17459
MUS-V (GENG ET AL., 2024)	MUSCLE	SAMPLED VIDEO	3114

US-JEPA: A Joint Embedding Predictive Architecture for Medical Ultrasound

DATASET NAME	ANATOMY	FRAME TYPE	FRAME COUNT
MUSCLEUS (MEIBURGER, 2021)	MUSCLE	STATIC	8169
UBPD (DING ET AL., 2022)	NERVE	SAMPLED VIDEO	955
ULTRASOUNDCASES.INFO	NERVE	STATIC	458
NERVEUS (MONTOKA ET AL., 2016)	NERVE	STATIC	11143
OVARIANUS (BORNA ET AL., 2025)	OVARIAN	STATIC	301
PCOS_US (CHOUDHARI & KORDE)	OVARIAN	STATIC	3841
RADIMAGE.NET	OVARIAN	STATIC	3595
ULTRASOUNDCASES.INFO	PANCREAS	STATIC	1506
LEPSET (LI ET AL., 2023)	PANCREAS	STATIC	11493
105US (HANN ET AL., 2017)	PANCREAS	STATIC	105
RADIMAGE.NET	PANCREAS	STATIC	21645
RADIMAGE.NET	PORTAL VEIN	STATIC	769
PROSTATETRUS (BAUM ET AL., 2023)	PROSTATE	VOLUME	5037
PROSTATE-MRI-US-BIOPSY (NATARAJAN ET AL., 2020)	PROSTATE	VOLUME	219484
MUPSD (SHAO & BRISBANE, 2024)	PROSTATE	VOLUME	2910
ULTRASOUNDCASES.INFO	REPRODUCTIVE	STATIC	3446
RADIMAGE.NET	SPLEEN	STATIC	6520
ULTRASOUNDCASES.INFO	SPLEEN	STATIC	1207
USANOTAI	SPLEEN	STATIC	61
RADIMAGE.NET	THYROID	STATIC	92598
SEGTHY (KRÖNKE ET AL., 2022)	THYROID	VOLUME	136243
ULTRASOUNDCASES.INFO	THYROID	STATIC	2011
THYD2 (HOU ET AL., 2024)	THYROID	STATIC	8489
DDTI (PEDRAZA ET AL., 2015)	THYROID	STATIC	610
TG3K (GONG, 2026)	THYROID	STATIC	3585
TN3K (GONG, 2026)	THYROID	STATIC	3493
STANFORD THYROID CINE (YAMASHITA ET AL., 2022)	THYROID	VIDEO	17412
RADIMAGE.NET	UTERUS	STATIC	13312
YANG (TIANTIAN YANG, 2023)	UTERUS	STATIC	1973

A.2. Downstream Datasets

Below, we provide a more detailed description of each downstream dataset, summarized in Table 4. We use the publicly available UltraBench tool to setup the datasets and corresponding training, validation and test splits. We contribute two more datasets, BUSBRA and TN5000, to UltraBench for a more comprehensive downstream evaluation.

Annotated Ultrasound Liver (AUL): The Annotated Ultrasound Liver (AUL) dataset is a collection of 2D liver ultrasound images introduced for research on automated liver lesion analysis and mass characterization (Xu et al., 2023). It comprises images acquired from distinct patients and includes expert annotations delineating the liver boundary and, when present, lesion contours. Each image is additionally assigned a clinical label reflecting the presence and type of focal liver mass, enabling both region-aware and image-level learning. The dataset spans a wide range of image resolutions and visual appearances, capturing realistic variability in ultrasound acquisition and anatomy. We use AUL for a supervised image-level mass classification downstream task with three classes: malignant mass, benign mass, and normal (no mass). The full dataset contains 735 images in total. We follow a fixed split consisting of 529 images for training, 59 for validation, and 147 for testing, ensuring that all splits remain patient-independent and preserve the original class distribution.

Butterfly: The Butterfly dataset was released by Butterfly Network for the 2018 MIT Grand Hack to promote research in point-of-care ultrasound understanding (Butterfly Network, 2018). It comprises ultrasound images acquired using the Butterfly iQ device from multiple anatomical regions across 31 patients, reflecting the diversity and variability encountered in real-world bedside imaging. Each image is labeled according to the anatomical site being examined, enabling supervised learning for anatomical recognition in ultrasound. We use the Butterfly dataset for a supervised organ classification downstream task with nine classes: Morison’s pouch, bladder, heart (parasternal long-axis view), heart (four-chamber view), heart (two-chamber view), inferior vena cava, carotid artery, lungs, and thyroid. The dataset contains a total of 41,076 images, with 28,053 images used for training, 6,272 for validation, and 6,751 for testing. All splits are patient-independent to prevent data leakage and ensure fair evaluation.

Fatty Liver: The Fatty Liver dataset consists of B-mode liver ultrasound images introduced for studying automated detection of hepatic steatosis and non-alcoholic fatty liver disease (NAFLD) (Byra et al., 2018). The dataset includes images acquired from multiple patients with expert clinical labeling based on the presence of fatty infiltration in the liver parenchyma. It has been widely used to evaluate representation learning and transfer learning methods for liver ultrasound analysis, particularly in low-data clinical settings. We use this dataset for a supervised image-level fatty liver discrimination downstream task with two classes: normal liver and NAFLD. The dataset contains a total of 550 images, drawn from 55 patients. We use 390 images for training, 50 for validation, and 110 for testing. All splits are patient-independent to ensure a fair assessment of generalization performance.

GBCU: The Gallbladder Cancer Ultrasound (GBCU) dataset was introduced to support research on automated gallbladder lesion characterization from abdominal ultrasound images (Basu et al., 2022). It consists of expert-annotated images collected from a diverse patient cohort and labeled according to underlying pathology, enabling supervised learning for clinically relevant gallbladder cancer assessment. The dataset captures a range of normal and diseased presentations and has been used to benchmark deep learning methods for malignancy discrimination in ultrasound. We use GBCU for a supervised image-level lesion malignancy classification downstream task with three classes: normal, benign, and malignant. The full dataset contains 1,255 images in total. We use 1,019 images for training, 114 for validation, and 122 for testing. The original dataset provides a fixed train–test split with no patient overlap; the validation set is created by further splitting the training data, as patient identifiers are not available to enforce strict separation.

MMOTU: The Multi-Modality Ovarian Tumor Ultrasound (MMOTU) dataset was introduced to facilitate research on ovarian tumor analysis using ultrasound and contrast-enhanced ultrasound imaging (Zhao et al., 2023). It provides expert annotations and diagnostic labels for a diverse set of ovarian pathologies, supporting both localization and classification tasks. In this work, we consider only the 2D ultrasound images and associated labels, focusing on image-level learning for ovarian tumor characterization. We use MMOTU for a supervised multi-class image-level tumor classification downstream task with eight classes: chocolate cyst, serous cystadenoma, teratoma, theca cell tumor, simple cyst, normal ovary, mucinous cystadenoma, and high-grade serous cystadenocarcinoma. The dataset contains 1,469 images in total. We use 800 images for training, 200 for validation, and 469 for testing. The original dataset provides a fixed train–test split, and the validation set is obtained by further splitting the training data, as patient identifiers are not available to enforce strict patient-level separation.

POCUS: The Point-of-Care Ultrasound (POCUS) dataset was introduced to support automated diagnosis of lung pathologies, particularly COVID-19, from bedside ultrasound imaging (Born et al., 2021). It aggregates lung ultrasound data acquired using convex and linear probes from multiple sources, reflecting real-world variability in point-of-care acquisition. The dataset has been widely used to benchmark deep learning methods for pulmonary disease recognition in ultrasound under heterogeneous data conditions. We use POCUS for a supervised image-level lung pathology classification downstream task with three classes: healthy, pneumonia, and COVID-19. Following the preprocessing protocol described in the original work, we use 29 convex-probe images and extract frame-level samples from 124 convex-probe videos while grouping frames by video to avoid data leakage across splits. The resulting dataset contains 2,064 images in total, with 1,444 images used for training, 177 for validation, and 443 for testing, ensuring strict separation at the video level.

BUSBRA: The BUS-BRA (Breast Ultrasound Brazil) dataset was introduced to support the development and standardized evaluation of computer-aided diagnosis systems for breast ultrasound imaging, with an emphasis on clinically meaningful annotations and reproducible benchmarking (Gómez-Flores et al., 2024). It consists of anonymized breast ultrasound images acquired from female patients during routine clinical examinations and includes expert-provided lesion delineations and biopsy-confirmed pathology labels. In addition to image-level diagnostic labels, the dataset incorporates BI-RADS assessments assigned by an experienced ultrasonographer, enabling research across multiple levels of breast cancer risk stratification and lesion characterization. The dataset has been designed to facilitate fair comparison of learning-based methods by providing well-defined partitions and comprehensive annotations commonly required in breast CAD pipelines. We use BUSBRA for a supervised image-level tumor malignancy classification downstream task with two classes: benign (722) and malignant (342). The dataset contains 1,064 images in total. We use 765 images for training, 86 for validation, and 213 for testing.

TN5000: The TN5000 dataset was introduced to enable large-scale research on automated thyroid nodule analysis from ultrasound imaging, with a particular emphasis on malignancy assessment (Zhang et al., 2025a). It comprises expertly curated ultrasound images of thyroid nodules collected through a rigorous process of data selection and annotation. Each image is paired with structured annotations following a PASCAL VOC-compatible format, where nodules are explicitly labeled and localized, allowing both region-aware modeling and image-level learning. Diagnostic labels are derived from

Table 4. Comprehensive statistics of the downstream datasets, including organ, task description, number of classes and data splits.

DATASET	ORGAN	TASK DESCRIPTION	CLASSES	TOTAL	TRAIN	VAL	TEST
TN5000	THYROID	NODULE MALIG.	2	5000	3500	500	1000
FATTY LIVER	LIVER	FATTY LIVER DIS.	2	550	390	50	110
POCUS	LUNG	PNEUMONIA, COVID	3	2064	1444	177	443
BUTTERFLY	MULTI	ORGAN DETECTION	9	41076	28053	6272	6751
GBCU	GALLBLADDER	LESION MALIG.	3	1255	1019	114	122
AUL	LIVER	MASS MALIG.	3	735	529	59	147
MMOTU	OVARY	TUMOR MALIG.	8	1469	800	200	469
BUSBRA	BREAST	TUMOR MALIG.	2	1064	765	86	213

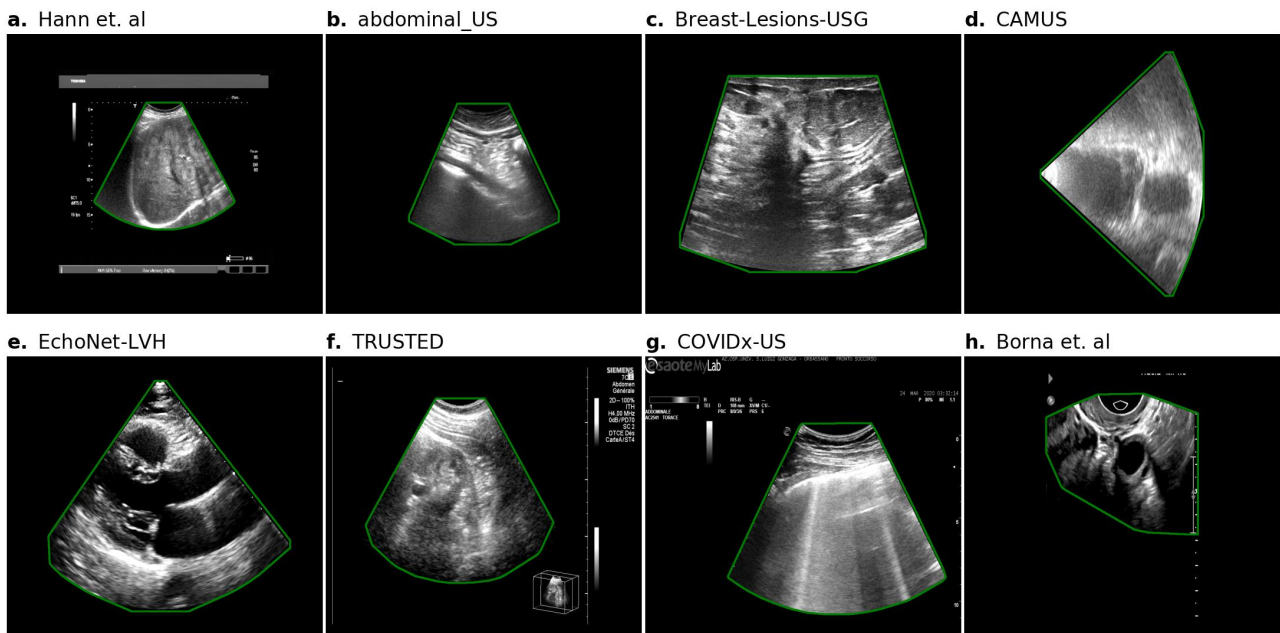


Figure 5

clinical assessment, and the dataset was intentionally constructed to reduce bias by maintaining a relatively balanced representation of benign and malignant cases at scale. TN5000 has been widely adopted for benchmarking deep learning approaches for thyroid cancer detection due to its size, standardized organization, and clear labeling scheme. We use TN5000 for a supervised image-level thyroid nodule malignancy classification downstream task with two classes: benign and malignant. The dataset contains a total of 5,000 images, including 3,572 malignant nodules and 1,428 benign nodules. We use 3,500 images for training, 500 for validation, and 1,000 for testing.

B. US region conditioning (USrc)

B.1. Image and USrc Mask Examples

In Figure 5, we have picked 8 datasets to include examples of images and the corresponding USrc mask. The USrc mask generated by our image processing algorithm is outlined in green and demonstrates the quality of the USrc mask generation.

Table 5. Shared pre-training hyperparameters for US-JEPA and USrc-JEPA. The models differ only in their use of ultrasound region conditioning.

CONFIGURATION	VALUE
<i>Architecture</i>	
ENCODER BACKBONE	VIT-BASE
PREDICTOR DEPTH	12
PREDICTOR EMBEDDING DIM	384
PREDICTOR TARGET DIM	768
<i>Data & Augmentation</i>	
INPUT SIZE	224×224
CROP SCALE	[0.6, 1.0]
AUGMENTATIONS	H/V FLIP, BLUR, ARTIFICIAL SPECKLE, CONTRAST
BATCH SIZE	128
<i>Masking (JEPA)</i>	
PATCH SIZE	16
CONTEXT MASKS (NUM, SCALE)	1, [0.85, 1.0]
TARGET MASKS (NUM, SCALE)	4, [0.075, 0.125]
ASPECT RATIO	[0.75, 1.5]
MIN. PATCHES KEPT	10
<i>Optimization</i>	
OPTIMIZER	ADAMW
TOTAL EPOCHS	100
WARMUP EPOCHS	10
BASE LEARNING RATE (LR)	5.0×10^{-5}
START \rightarrow FINAL LR	$5.0 \times 10^{-6} \rightarrow 5.0 \times 10^{-7}$
LR SCHEDULE	COSINE DECAY WITH LINEAR WARMUP
WEIGHT DECAY \rightarrow FINAL WD	0.04 \rightarrow 0.4
EMA MOMENTUM	[0.996, 1.0]

C. Training Details

C.1. Pretraining Parameters

We exclusively hold out 5% of the entire pretraining dataset to use as validation. For our downstream experiments, we evaluate the epoch checkpoint that gets the lowest validation loss during pretraining. All pretraining parameters are detailed in Table 5.

C.2. Downstream Parameters

We perform downstream evaluation by training a randomly initialized linear layer on top of the frozen encoder backbone. We utilize early stopping based on the validation loss with a patience of 15 epochs to prevent overfitting. The remaining parameters are detailed in Table 6.

D. Few-Shot Scaling for Linear Probe Extended

In Figure 6 we include the comprehensive few-shot scaling experiments. For all of our baselines we perform few-shot scaling across five random seeds to see how performance changes on each downstream. In the main paper, we only compare against URFM and USFM because they were the most competitive baselines.

E. Robustness to Domain-Specific Corruption Details

E.1. Extended Results

In Figure 7 we include the complete results for the OOD robustness experiment. We show the performance degradation for US-JEPA, USrc-JEPA, URFM and USFM with worsening levels of blur, contrast reduction and artificial speckle corrupting downstream test set images during probe evaluation.

Table 6. Hyperparameters for downstream linear probing on UltraBench datasets.

CONFIGURATION	VALUE
OPTIMIZER	ADAMW
BASE LEARNING RATE	1.0×10^{-3}
WEIGHT DECAY	1.0×10^{-4}
BATCH SIZE	32
INPUT SIZE	224×224
LOSS FUNCTION	CROSS-ENTROPY
LR SCHEDULE	COSINE ANNEALING
MAX TRAINING EPOCHS	150
EARLY STOPPING PATIENCE	15 EPOCHS

E.2. Formulas for Corruptions

To simulate ultrasound imaging artifacts, we define three corruption functions $C(I, \epsilon)$ where I is the input image and ϵ is the severity level ranging from 1 to 3.

Gaussian Blur: Gaussian blur is modeled as the convolution of the image I with a Gaussian kernel G , where the standard deviation σ is controlled by the severity ϵ :

$$I_{blur} = I * G_{\sigma} \quad \text{where } \sigma = \epsilon$$

The discrete kernel size for G is adjusted to $2\lfloor 2\epsilon \rfloor + 1$ to ensure the Gaussian distribution is properly captured.

Contrast Depletion: This corruption shrinks intensities toward the median brightness μ_{med} of the pixels defined by the USrc mask:

$$I_{contrast} = \mu_{med} + \alpha(\epsilon) \cdot (I - \mu_{med})$$

where the depletion factor α decreases as severity increases ($\alpha \in \{0.7, 0.5, 0.3\}$), effectively making anatomical boundaries less visible.

Correlated Speckle Noise: Speckle is modeled as multiplicative noise. The raw Gaussian noise η is spatially correlated via a smoothing kernel K before being applied.

$$I_{speckle} = I \cdot (1 + \eta_{corr})$$

The noise characteristics are functions of severity ϵ :

- Magnitude: $\eta \sim \mathcal{N}(0, \sigma_{noise}^2)$ where $\sigma_{noise} = 0.35\epsilon$.
- Correlation: $\eta_{corr} = \eta * K_{size}(\epsilon)$, where the kernel size K_{size} increases with ϵ to simulate larger speckle grains at higher severity.

E.3. Qualitative Examples

In Figure 8, we have included a qualitative example of the varying severities for each corruption on one example image from the AUL downstream dataset.

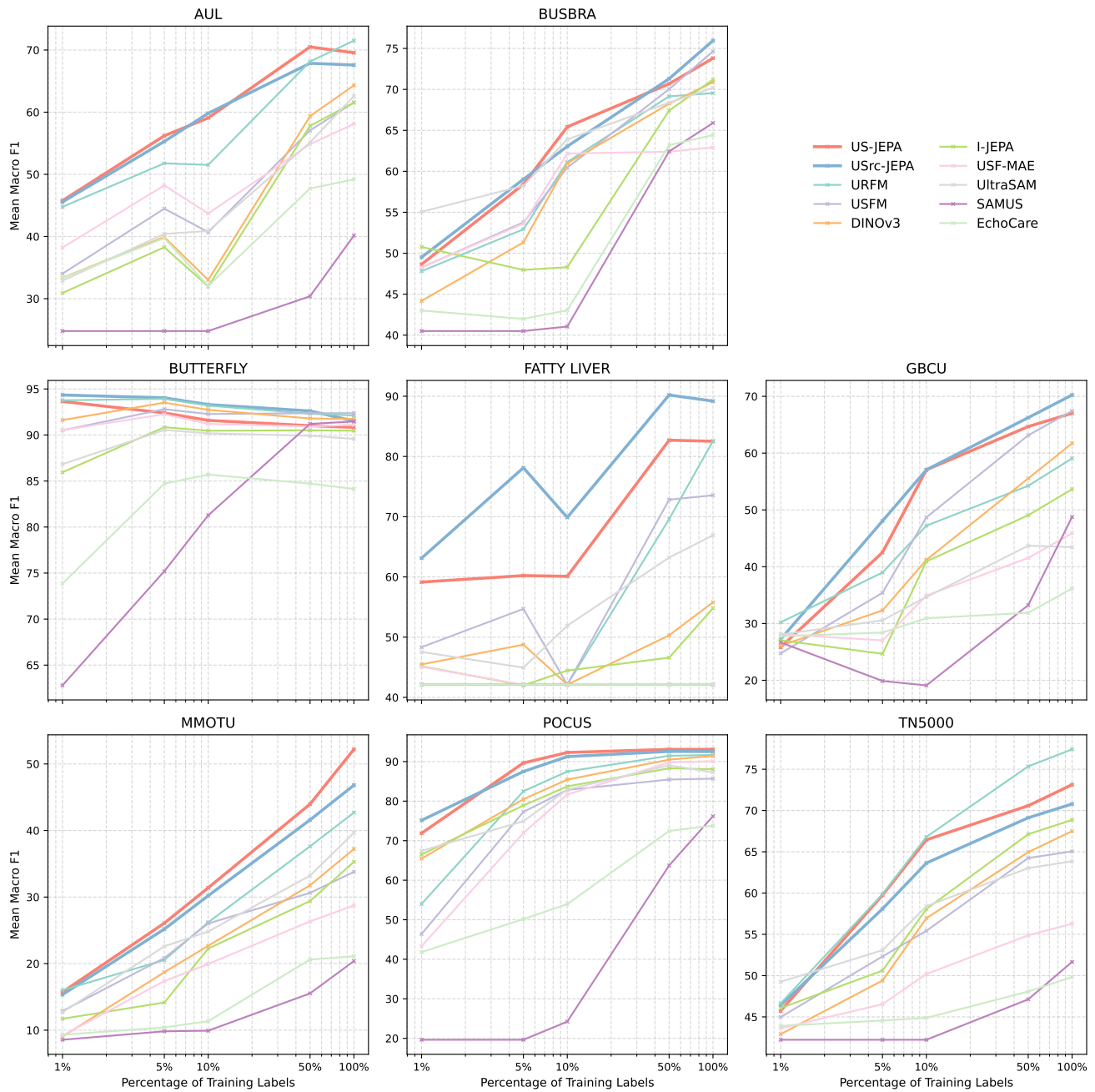


Figure 6. Few-shot classification robustness across all datasets. Here the test set evaluation for linear probe tuned with varying percentages of training data are shown for all models.

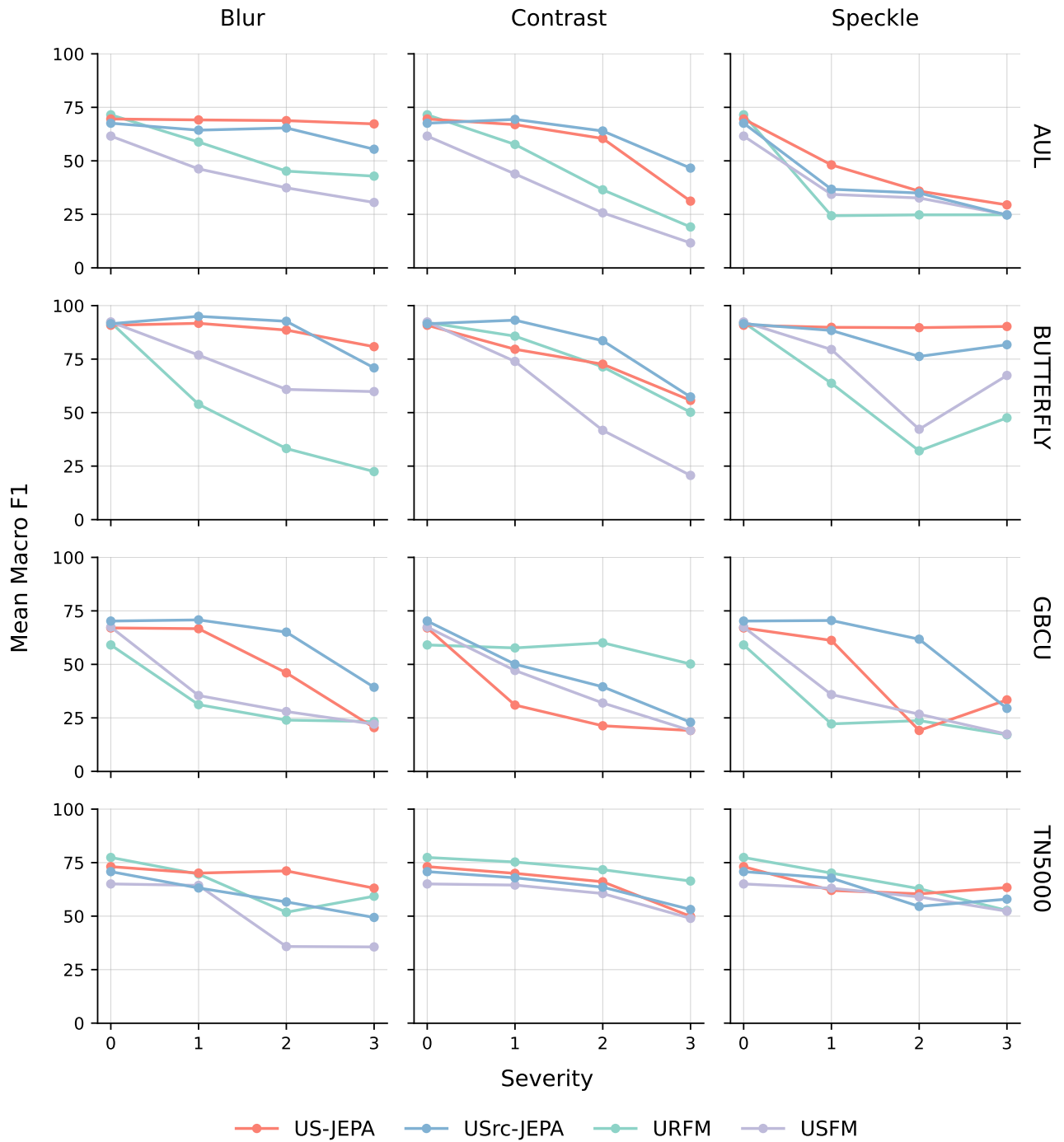


Figure 7. OOD robustness results for remaining 4 downstream datasets.

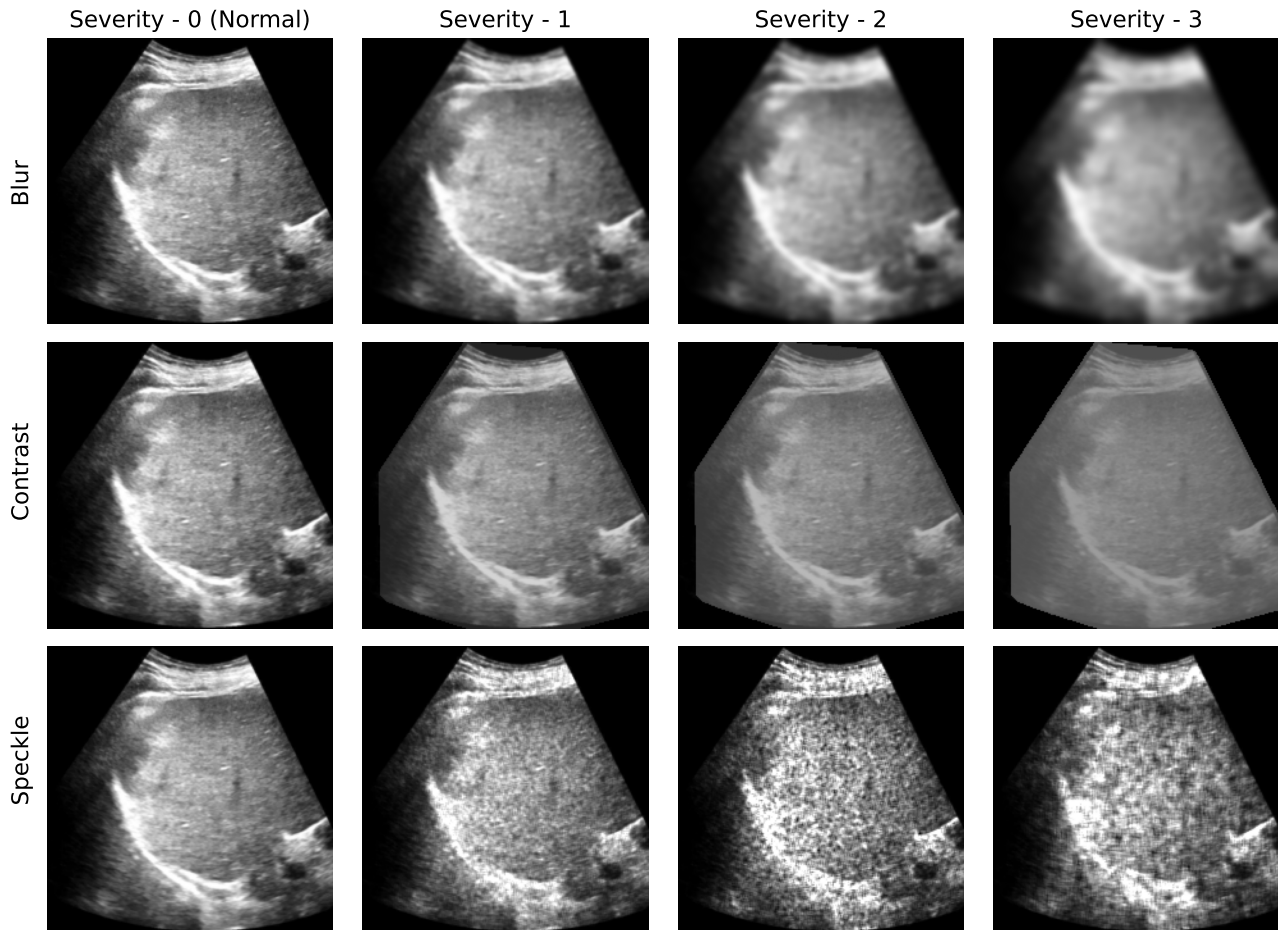


Figure 8. Different corruptions at three severity levels applied to a liver ultrasound from AUL dataset.